Electronic Supplementary Material (ESI) for Energy & Environmental Science.

Supplementary Information

Advanced Li Metal Anode by Fluorinated Metathesis on Conjugated Carbon Networks

Yong Jun Gong,‡[a] Seonmi Pyo,‡[a] Hyunjin Kim,[ab]Jinil Cho,[a] Heejun Yun,[a] Heebae Kim,[a], Seokgyu Ryu,[c] Jeeyoung Yoo[c] and Youn Sang Kim[ad*]*

[a.]Program in Nano Science and Technology, Graduate School of Convergence Science and Technology, Seoul National University, Gwanak-ro 1, Gwanak-gu, Seoul 08826, Republic of Korea

[b] Korea Research Institute of Chemical Technology, 141 Gajeong-ro, Yuseong-gu 34114, Republic of Korea

[c.]Department of School of Energy Engineering, Kyungpook National University, Daehak-ro 80, Buk-gu, Daegu 41566, Republic of Korea

[d.]School of Chemical and Biological Engineering, College of Engineering, Seoul National University, Gwanak-ro 1, Gwanak-gu, Seoul 08826, Republic of Korea

* Corresponding author

Prof. Youn Sang Kim - E-mail: younskim@snu.ac.kr, Tel: +82-2-880-7411 (Lead contact)

Prof. Jeeyong Yoo - E-mail: jyoo@knu.ac.kr, Fax: +82-53-950-8979, Tel: +82-53-950-8976

Experimental procedures.

Preparation of the graphene-coated-fibers: Graphene powder was purchased from Graphene Supermarket (graphene nanopowder 99.9%, AO-2), and 3-methoxy-3-methyl-1-butanol (MMB) was purchased from Alfa Aesar (98+%). Commercial phenol-formaldehyde resin (PR) was used as binder. Carbon black (CB) (Timcal, super-P) and commercial activated carbon (AC) were used as other extended conjugated carbon network (CCN) materials. To prevent hydration, all carbon materials were stored in a convection oven (120 °C) before use. Before the mixture preparation, graphene powder was subjected to physical friction with two 5 mm Zr-ball and five 1 mm Zr-ball for 30 min at 2000 rpm in a 15 mL PTFE Teflon jar to prevent flake agglomeration and to ensure the uniformity of flakes by homogenizer (Thinky Mixer AR-100). This grinding process had been carried out five times. After that, graphene powder and phenol-formaldehyde resin were mixed with a weight ratio of 13:4, and then this high-viscosity mixture was diluted to 70 wt% in MMB solvent and dispersed homogeneously for 20 minutes by tip sonication (VC-750, Sonics & Materials, Inc.). The dispersion using by tip sonication was done three times. As-prepared graphene paste was painted on a paper-mill-aramid (Mitsubishi, paper-mill-aramid: HP3015, 30 μm thickness) by brush, and the graphene coated paper-mill-aramid was dried at 150 °C for 8 h in a convection oven. The carbon black- and the activated carbon-coated paper-mill-aramid were also prepared and painted by the same method, and dried at the same condition. After drying, the graphene coated paper-mill-aramid was attached to the uncoated paper-mill-aramid by applying a pressure of 30 MPa for 1 h at 50 °C by a hot-press. During this process, a trace amount of acetone and ethanol was drop-casted on the uncoated paper-mill-aramid. Paper-mill-aramid was a structure of fibers woven together using polyester and cellulose as adhesives. So, when the coated aramid was on the uncoated aramid wetted with acetone and ethanol, sufficient temperature and pressure were applied, making it to be easily attached and not to fall apart from each other. Finally, a double layer separator of about 40 ± 2 μm thickness was obtained. The resistance of the coated side was about 25 ~ 32 Ω cm^{-1} (graphene; 25 Ω cm^{-2}, carbon black and activated carbon; 26 ~ 32 Ω cm^{-2}) and the uncoated side was completely insulating.

Preparation of $LiFePO_4$ to high C-rate test: $LiFePO_4$ (LFP) nanoparticles were firstly prepared as a cathode material by the solvothermal synthesis method and were secondary processed by additional treatment to a high C-rate test.[40] Lithium hydroxide monohydrate ($LiOH\cdot H_2O$, 99%), phosphoric acid (H_3PO_4, 85%), and iron sulfate heptahydrate ($FeSO_4\cdot 7H_2O$, 99%) were purchased from Sigma Aldrich, ACROS, and Alfa Aesar, respectively. These materials were used as precursors in the stoichiometric ratio of 2.7:1:1.5, respectively. For the solvothermal synthesis, appropriated quantity of $LiOH\cdot H_2O$ was dissolved in 45 mL of commercial ethylene glycol (99%). H_3PO_4 was added dropwise into the solution of the previous step under stirring. $FeSO_4\cdot 7H_2O$ was dissolved in 30 mL of ethylene glycol and then the $LiOH\cdot H_2O$ solution was added into the iron sulfate solution under stirring. The obtained green suspension was transferred into a Teflon-lined stainless steel autoclave and then heated at 180 °C for 10 h. After the heating process, the autoclave was cooled at room temperature. The obtained gray precipitates were washed with ethyl alcohol and deionized (DI) water for the several times. The LFP residues were dried in the freeze drier and the nanoparticle state of the LFP powder was finally obtained. For a high C-rate test, LFP synthesized through the above steps was additionally processed with N-doped carbon (NC) and reduced graphene oxide (rGO). Graphene oxide (GO) was synthesized by a modified Hummers' method.[69] Dopamine hydrochloride and Tris-buffer were purchased from Sigma Aldrich. As-prepared LFP powder was dispersed in Tris-buffer solution (10 mM) by sonication. Then, dopamine hydrochloride (3 mg mL^{-1}, 200 mL H_2O) was added to the suspension of the previous step and stirred for 15 min. GO suspension (3 wt% in H_2O) was added into the dopamine solution for 10 min. After 5 min of reaction, the suspension of LFP, dopamine, and graphene oxide suspension was washed three times with DI water and dried at 70 °C in an oven for 10 h. The collected LFP@polydopamine@GO composite was calcined at 700 °C for 5 h in Ar-filled Swagelok container to form LFP@NC@rGO. All LFP used in this experiment were applied to Li/LFP cell after the post-treatment with N-doped carbon and reduced graphene oxide. In the coin cell fabrication, LFP cathode was prepared by mixing the as-prepared active materials with carbon black (CB) as a conductive material (Timcal, super-P), and poly(vinylidenefluoride) as a binder (PVDF, Kynar HSV900). This mixture was dissolved in commercial N-methyl-2-pyrrolidone (NMP, 99%) at a concentration of 7 wt% in a weight ratio of 70:15:15 (LFP:CB:PVDF). The mixed slurry was coated onto an aluminum foil current collector and dried at 120 °C under vacuum for 10 h. In the pouch cell fabrication, as a binder, poly(vinylidene fluoride-co-hexafluoropropylene) (PVdF-HFP; M_w = 400000 and M_n = ~130000 g mol^{-1}, Sigma Aldrich) was used instead of PVDF.[41,42] The mixed slurry was drop-casted on a Teflon plate. After drying, the free-standing LFP was peeled off and transferred to a freeze drier to obtain the final flexible LFP cathode.

The initialization steps of $LiFePO_4$ interface: The LFP cathode made for the high C-rate test undergone a two-stage stabilization process for the initialization of the LFP interface before the cycling.[40] As-assembled Li/LFP cell undergone the rest stage for liquid electrolyte soaking for 24 h at room temperature. Then, as first stabilization process, Li/LFP cell was cycled five times at a 0.1 C-rate within a potential window of 2.0 to 4.2 V to the LFP interface for initialization. After that, as a second stabilization process, the Li/LFP cell was cycled five times at a 0.2 C-rate within a potential window of 2.5 to 4.2 V to the LFP interface for initialization. After the two stages of stabilization, the Li/LFP cell was tested within a potential window of 2.5–4.2 V *vs.* Li^+/Li. The loading density of the active materials was about 1.5 mg cm^{-2}, and testing temperature was 30 ºC.

Electrochemical measurement: The CR2032 coin cell was assembled with a Li/Cu asymmetrical cell, Li|Li symmetrical cell, and Li/$LiFePO_4$ cell using paper-mill-aramid separators (Mitsubishi, paper-mill-aramid: HP3015 - 30 μm thickness, HKMS50 - 50 μm thickness)) and 1M $LiPF_6$ (in EC/DEC/DMC =1/1/1 v/v/v) (Panax Etec Co. Ltd. STARLYTE or Simga Aldrich). HP3015 (30 μm) was used for the paste coating and for the uncoated aramid as separator in GAA system, and HKMS50 (50 μm) was used as the reference system and for the pencil drawing. Galvanostatic cycling measurements in the Li|Li symmetrical cell test were performed (1) at a current density of 5 mA cm^{-2} (1 mAh cm^{-2}), (2) at a high current density of 20 mA cm^{-2} (1 mAh cm^{-2}) as the rapid charging/discharging test, (3) at a high areal capacity and at a high current density of 20 mA cm^{-2} (20 mAh cm^{-2}).[23-26] The amount of Li plated was 0.00259 g under 1 mA cm^{-2} for 10 h. Based on this, the plated Li was 0.000259 g for 1 mA cm^{-2} for 1 h. Thus, 1.000258 mAh was set to 1 C-rate (3862 mAh g^{-1} × 0.000259 g). In Li/Cu asymmetric cell, Li foil was used as the counter electrode and the reference electrode. In symmetrical cell, Li metal foil (MTI Korea - 300 μm) was used as the working, counter, and reference electrode. In life span test, custom-made thin Li metal electrode on Cu was supplied by Welcos (thickness - Li; 30 μm and Cu; 10 μm). Galvanostatic cycling measurements in Li metal battery test were performed at 20 C-rates with LFP@NC@rGO. A commercial available pouch cell having a nominal dimension of 65 mm × 50 mm × 1.5 mm were assembled. LFP, Li metal and GAA were used as cathode, anode, and separator, respectively. GAA separator was used after soaking in the electrolyte for a sufficient time. All manufacturing processes were carried out in an Ar-filled glove box under vacuum with 0.1 ppm or less of oxygen and 1 ppm or less of humidity.

The resistance measurement: The sheet resistance was measured using a source meter (Keithley 2400). First, conductive silver paste was painted at vertices of Square-shaped GAA (the coated side). Electrode tip was contacted to sample and a current of 1 mA was applied to measure the voltage drop. The R_A value and R_B value obtained from this measurement were substituted into Van der Paw's law to get the sheet resistance.

X-ray photoelectron spectroscopy (XPS) analysis: X-ray photoelectron spectroscopy (Kratos, Axis Supra™) analysis was used to investigate the elemental species, binding state, and distribution of specific elements in the prepared sample. All samples, which were vertically cut to 0.8 cm × 0.8 cm specimens at the center by a razor blade, were measured without any additional treatment to observe the surface as it was in ultra-high vacuum (UHV) chamber under 5×10^{-10} torr and excited by monochromatic Al Kα radiation (1486.6 eV) source with operation at 15 kV. Reference and sample were analyzed using XPS equipment with higher resolution. The binding energy of XPS spectra was calibrated using a carbon peak (sp^2 C at 284.5 eV) as the reference, peak fitting of all spectra was undertaken on XPSPEAK4.1 program grounded the Shirley background and Lorentzian-Gaussian curve synthesis.

X-ray diffractometer (XRD) analysis: Carbon materials stored in a convection oven (120 °C) went through the same grinding process as in the process of making paste, and samples were scanned and recorded using an X-ray diffractometer (Smartlab, Rigaku) with an X-ray generator from 0 to 80 of 2θ (diffraction angle) using CuKα radiation under the following conditions: 40 kV and 30mA ($\lambda = 0.154$ nm). A pencil rod also went through the same grinding process, and its powder was scanned and recorded in the same way.

Electron microscope analysis: High resolution scanning electron microscopy (HR-SEM with JEOL Ltd) analysis and scanning transmission electron microscopy (Cs corrected STEM with Cold FEG, JEOL Ltd) analysis were carried out at 15 kV (SEM) and 80 kV (TEM). After electrochemical tests, the cells were carefully disassembled by de-crimping machine (MTI Korea MSK-110) in an Ar-filled glove-box. To prevent oxidation of surface of Li metal, Li metal is taken out from an Ar-filled glove-box while being immersed in an ionic liquid (1-Ethyl-3-methylimidazolium bis(trifluoromethylsulfonyl) imide, [EMI][TFSI]), and then SEM analysis was conducted. Other samples were sealed with Ar gas, and then taken out of the Ar-filled glove-box. For cross-sectional analysis of the GAA single strand fiber, a dual beam focused ion beam (FIB, Helios 5 UX, Thermofisher) equipment was used to prepare samples for TEM investigation.

Microscopic Fourier-transform infrared spectroscopy (FT-IR) analysis: For cross-sectional analysis of GAA and uncoated aramid fiber by microscopic FT-IR (Perkin Elmer), the coated side of GAA separator and the uncoated aramid fiber were cut using by the surface and interfacial characterizing analysis system (SAICAS, Daipla wintes). After the cutting process, the coated fiber of GAA separator and aramid fiber was scanned from 600 to 2000 cm^{-1}. The confirmation of graphene coating of the uncoated aramid fiber was scanned from 400 to 4000 cm^{-1} in normal mode.

Time-of-flight secondary ion mass spectrometer (TOF-SIMS) analysis: A time-of-flight secondary ion mass spectrometer (TOF.SIMS 5, ION-TOF) at a pressure below 3.8×10^{-9} Torr was used for analysis of the depth and 3D depth mapping of the chemical composition of Li metal anodes by the negative polarity. A Bi^+ (30 keV, 1 pA) ion beam was used as the primary source for detecting the composition of facile-section, and sputtering with a Cs^+ ion beam (2 keV, 150 nA) was used for depth profiling analysis (analysis area; $100 \times 100\ \mu\mathrm{m}^2$, etching area; $400 \times 400\ \mu\mathrm{m}^2$).

Zeta-potential measurements and Dynamic light scattering spectrophotometer (DLS): Graphene, carbon black, and activated carbon powders were subjected to physical friction with two 5 mm Zr-ball and five 1mm Zr-ball for 30 minutes at 2000 rpm in 15 mL PTFE teflon jar. Like the paste preparation, grinding process had been carried out five times. And powders were dispersed in water (DLS: ethyl alcohol) at an appropriated concentration by tip sonication for 20 minutes. Like the paste preparation, tip sonication also was done three times. After that, Zeta-potential and DLS were measured to each aqueous (DLS: ethyl alcohol) solution by electrophoretic light scattering spectrophotometer (Els z-1000, Otsuka Portal) and by dynamic light scattering spectrophotometer, respectively.

Atomic force microscopy (AFM) analysis: The thickness of graphene flake was investigated using AFM (XE100, PSIA).

Raman spectroscopy analysis: The graphene powder was characterized by Raman (DXR2xi, Thermo, USA).

Additional note 1. Galvanostatic cycling measurements in Li/Cu half-cell test

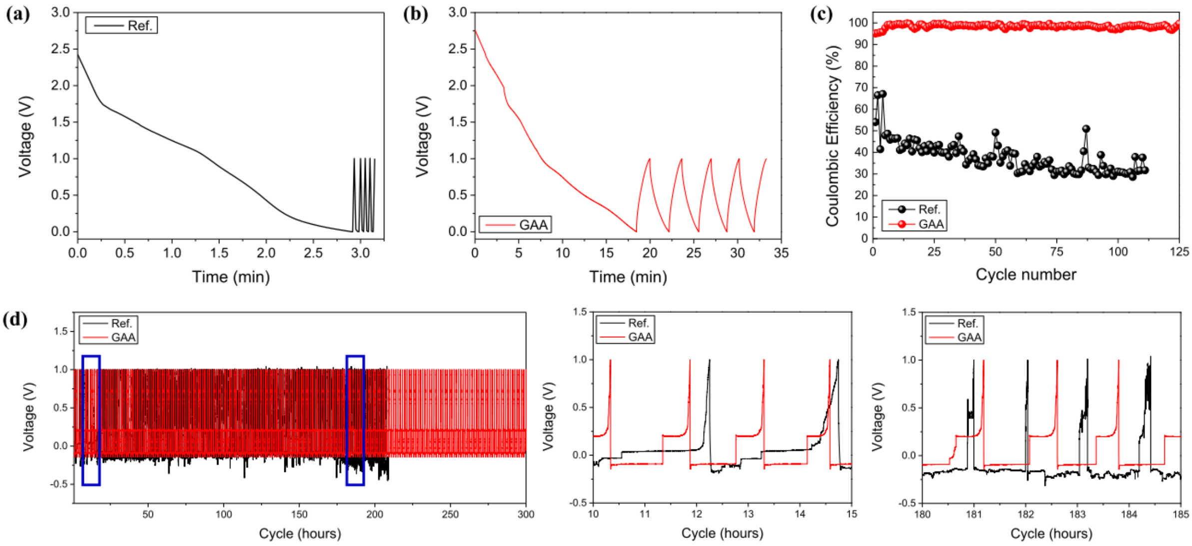

***Galvanostatic cycling measurements of Li/Cu asymmetric cell (half-cell).** Initialization process of (a) the reference system and (b) the GAA applied system. (c) Coulombic efficiency of Li/Cu asymmetric cell. (d) Time-voltage profiles of Li/Cu asymmetric cell for the reference system and the GAA applied system. the system is virtually a failure

Galvanostatic cycling measurements of a Li/Cu asymmetric cell (half-cell) structure were conducted to analyze the Li^+ ions plating/stripping behavior on the surface and assess the SEI structure stability when using GAA separator in a three-electrode system.[39] In Li/Cu asymmetric cell, a planar Cu foil served as the working electrode and Li foil served as both the counter electrode and the reference electrode. The structure of the reference system and the GAA applied system are as follows; the reference system - Li/aramid/Cu (black), the GAA applied system - Li/aramid/graphene-coated-fibers/Cu (red). To evaluate the stability of SEI formed in the GAA case, the graphene-coated-fibers side was put in contact with the planar Cu foil. Before the test, asymmetric cells (half-cell) were cycled 5 times from 0 to 1 V at a current density of 50 $\mu A\ cm^{-2}$ for initialization. The purposes of initialization were to remove any contamination on the surface, and to stabilize the interface and the initial SEI. During this initialization process, the plated Li^+ ion was partially consumed for the formation of initial SEI layer. Then, Li^+ ion was plated on the Cu foil (the working electrode) at a current density of 1 mA cm^{-2} (1 mAh cm^{-2}). Next, the polarity was reversed, and the plated Li on the Cu foil was stripped to Li foil (the counter and reference electrode) up to 1 V. In the reference system, since SEI was unstable, a new SEI was continuously formed in each cycle, consuming the Li^+ ion source; this led a low coulombic efficiency (the stripped Li^+ ion/the plated Li^+ ion) and a minimal capacity stripped at each cycle because no Li reservoir was employed. Therefore, the reference system was gradually degraded as the cycling continued. When less than only 30 % of coulombic efficiency appears, the system is virtually a failure. However, the GAA applied system showed the low cathodic overpotential in constant and regular shape when the cycle progressed. This indicates the SEI is stable due to the passivation by the GAA separator. Therefore, the GAA applied system exhibited the coulombic efficiency of >99% after the initial stages because only a little Li^+ ion source was consumed to form new SEI. These results prove that the GAA architecture can improve the structural stability of SEI formed on it, and GAA separator can help induces the stable SEI.

Additional note 2. Stepwise behavior of Li|Li symmetrical cell

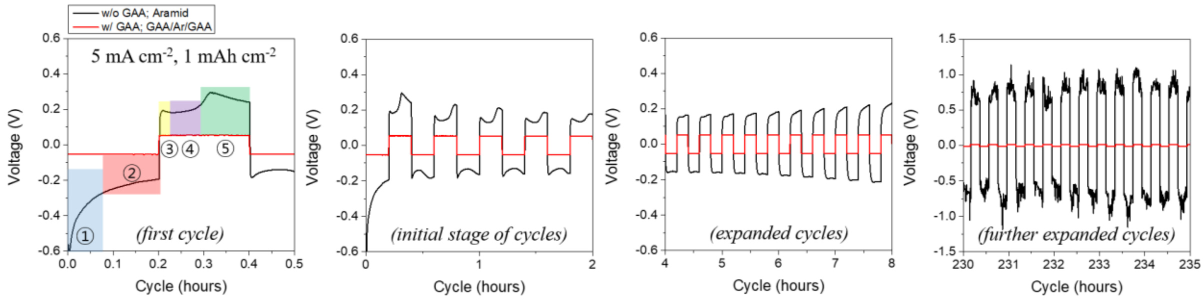

The voltage variation in the time-voltage profile, when current was applied to Li metal anode in the reference system, indicates the stepwise behavior according to the kinetics of each stage. And such kinetics is relied on the morphological surface changes of Li metal anode.[36-38] The initial stages of the cycle represent the peaking shape which is dependent on the spatially varying rate constant. In the first half-cycle of region 1, in the manufacturing process, the native oxide layer and the initial SEI layer spontaneously formed in both the reducing electrode and the oxidizing electrode induce the specific kinetic hindrance. And such layers interfere the Li^+ ions plating to the reducing electrode and the Li^+ ion stripping from the oxidizing electrode, contributing to the high overpotential at the beginning stage. In region 2, as the Li^+ ion plating progressed, the nucleation points, which can grow into the dendritic growth containing SEI, were formed on the surface of the reducing electrode, while SEI also was formed on the Li metal anode surface. In this stage, the dendritic growth took precedence over the formation of the nucleation point in the reducing electrode, and the pitting process is dominant in the oxidizing electrode. Thus, the overpotential gradually decreased from the initial maximum overpotential at the beginning stage. After the polarity is reversed, the reducing electrode and the oxidizing electrode were reversed. In second half-cycle of region 3, since the fluctuated surface with pits and the the dendritic growth of the nucleation point on the reducing electrode contributed to the activation barrier for Li^+ ion transfer, a convex graph shape appeared in the initial voltage. In this step, the nucleation point formation was dominant than the dendrite growth on the reducing electrode, and in the oxidizing electrode, the stripping from the dendrite was in preference to from bulk Li because of the short pathway. As the plating continued, the Li^+ ion movement pathway transitioned from the nucleation point formation to dendrite growth on the reducing electrode. After the pathway transition has occurred, the plating to the dendrite on the reducing electrode and the stripping from dendrite on the oxidizing electrode were dominant, and this kinetics was relatively fast. Besides, the Li which was newly deposited in the previous cycle did facilitate the stripping process on the oxidizing electrode. Thus, the minimum voltage was observed in region 4. All the Li deposited in the previous cycle were stripped and the active Li source was exhausted, and then, the Li source was changed from dendrite to bulk Li. Therefore, an energy barrier was required in the stripping process from bulk Li under the SEI layer, increasing overpotential in region 5. In this process, the Li dendrite, of which the active Li was depleted, became the electrically isolated Li as the resistance element. In the tail area of region 5, the pathway transition reoccurred from the bulk Li to the pits on the oxidizing electrode, reducing the overpotential. Like this, a minimum amount of the inactive layer, which was accumulated on the electrode, did induce the fast quasi-steady-state condition during the initial cycles; hence, the time-voltage profile was mainly determined by the spatially varying rate constant. This process was continuously repeated as the cycle progressed, accumulating more inactive layer from pits, dendrite, and isolated Li on the Li metal anode surface, which established a large concentration gradient. Therefore, as the cycle progresses, the effective diffusion coefficient became smaller. In the expanded cycles, since the thick inactive materials layer made tortuous pathway across the electrode/electrolyte interphase, the Li^+ ion transport was impeded by this thick inactive layer. And the large Li^+ ion concentration difference between the reducing electrode and the oxidizing electrode made that the mass transport be the dominant kinetics in the expanded cycles. This interfacial concentration variation was accompanied by an overpotential increase and the dynamic concentration gradient reached its quasi-steady-state equilibrium with the arc shape plateau of the time-voltage profile in the half cycle. When continuing the cycle, in the further expanded cycles, the brittle nature of the unstable SEI resulted in cracks on its surface and the exfoliated dendrites re-exposed the underneath Li to fresh electrolyte. The exposed pristine Li consumed the fresh electrolyte and generated the new SEI. These undesirable interfacial reactions induced the increase of the ohmic potential drop and the irregular anodic polarization curve, eventually causing the cell failure. Due to this characters of Li as an anode, at a current density above 0.5 mA cm^{-2}, suppressing the Li dendrite for a long-time is a hard task; besides, the when current is applied, controlling the unstable SEI formation by the dendrite nucleation and the pits is challengeable as well.[5,70]

Additional note 3. semi-ionic C−F bond

The C–F bond characters of the fluorinated conjugated carbon network (CCN) materials are depending on the fluorine/carbon ratio (or stage number, C_x/F).[71-73] A decreased fluorine (the increased stage number) makes the C–F bond to have the properties of the ionic bond. Adversely, an increased fluorine (the decreased stage number) makes the covalent C–F bond.[71] The environment for the formation of commonly known semi-ionic C−F bonds is the fluorination of graphene. During the fluorination process of graphene, fluorine has two competitive reactions: (i) F^- anion reacts with the carbon atom of graphene to form a covalent C−F bond, where sp^3 carbon atom binds with F^- anion, thereby forming the buckled carbon sheet by fluorine. (ii) F^- anion reacts with the carbon atom of graphene to form a semi-ionic C−F bond, where sp^2 carbon atom binds with F^- anion, maintaining the planar carbon sheet without structure variation. The semi-ionic C−F bond is mainly formed by the chemical reaction of (ii) and shows its electronic configuration changes from sp^2 to sp^3, arising bond angle distortions.[45] Therefore, the semi-ionic C–F bond has the intermediate state between the covalent bond and the ionic bond; it represents a lower bonding order and a longer bonding length than the covalent C–F, and it also has a chemically reactive property than the covalent bond without the ionization.[74] This nature of the semi-ionic C–F bond results from the binding state of fluorine atom, which is connected to the CCN as a hyperconjugation state, and results from the low the bonding dissociation energy (BDE) of fluorine atom to graphene.[50, 75-77] This feature differs from the poly(tetrafluoroethylene) (PTFE) or poly(vinylidene-fluoride) (PVDF) derivatives containing of poly(carbon mono- or di- fluoride; low stage number), which are considered as inert due to their high bonding dissociation energy.[78] Moreover, the fluorine/carbon ratio (stage number) affects the conductivity. As the stage number (C_x/F) increases from 2 to 5 or more, the resistance decreases exponentially from 10^7 Ω cm to 10^{-3} Ω cm, showing a sufficient conductivity, unlike PTFE or PVDF which are considered as insulators.[55]

In the proposed system, the semi-ionic C–F bond was formed also along the CCN materials in the coated fibers. When a current was applied, the reduction atmosphere was created in the electrode and the coated fibers in contact with the electrode. Then, in the decomposition process of an electrolyte, PF_6^- anion of $LiPF_6$ electrolyte was decomposed into PF_5 and F^- anion. Especially, when PF_6^- was decomposed in a solvent having polar, compact, and high dielectric constants properties, such as ethylene carbonate (EC) in this system, the resulting PF_5 was further stabilized and optimized by those solvent molecules in solvation process. In detail, because of the increase of PF_5 stability, the hybrid orbital of the fluorine coupled to the phosphorous of PF_6^- simultaneously could be dissociated during the decomposition process, and fluorine radical exists in an instantaneously intact state. At this time, the graphene is electron-rich state and then bind with sp^2-hybridized carbon in the CCN. Since only some of C atoms changed their electronic configuration from sp^2 to sp^3, the semi-ionic C–F bond was formed; fluorinated metathesis. Based on the atomic percent in EDS lining data, acquired at the site between the graphene with a clear lattice fringe and the lattice relaxation area (where carbon and oxygen interact chemically), the stage number was higher than 5. This indicates a low resistance and a low BDE of the partially fluorinated CCN. Therefore, the properties of the semi-ionic C–F bond, where the fluorine is partially connected to the CCN, were as follows: chemical reactivity from the low-order carbon-fluorine, conductivity from the high stage number, $C^{\delta+}$–$F^{\delta-}$ charge polarization from the high electronegativity of fluorine atom, and the low bonding dissociation energy of fluorine atom to graphene. This can lead to the unique fluorine-doped surface from the interaction between fluorine and carbon. Therefore, Li^+ ions can plate on the partially fluorinated sites of the CCN with the conductive property in the coated fiber,[56] the semi-ionic C–F bond met Li^+ ion flux to generate LiF, as the key material of stable SEI.

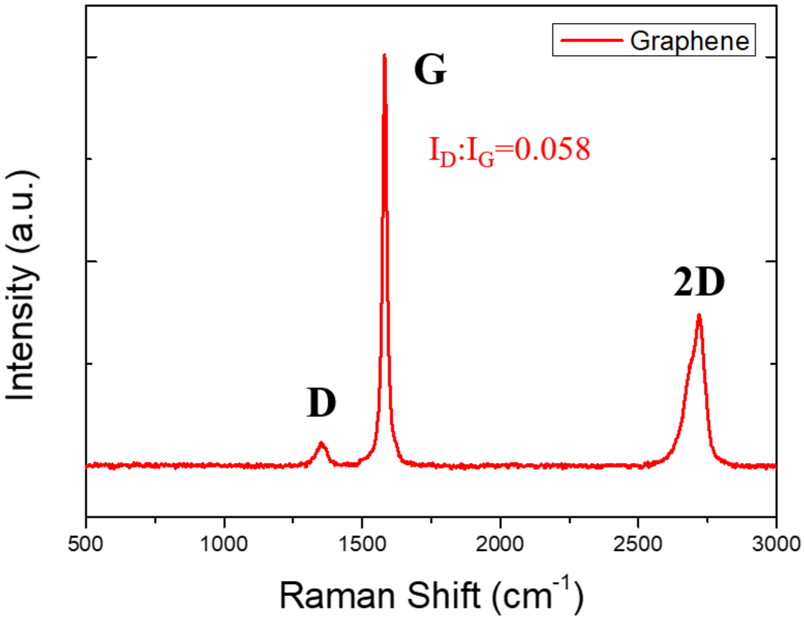

Figure S1. Raman spectroscopy of graphene. Raman spectroscopy clearly reveals the highly ordered nature of graphene, showing an I_D/I_G ratio of 0.058 and its sharp 2D peak.[62]

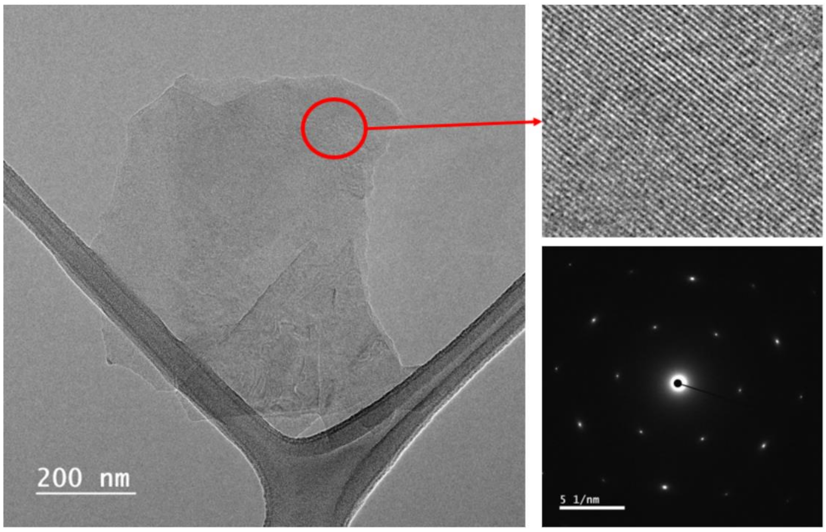

Figure S2. TEM image of graphene and its selected area electron diffraction (SAED) pattern.

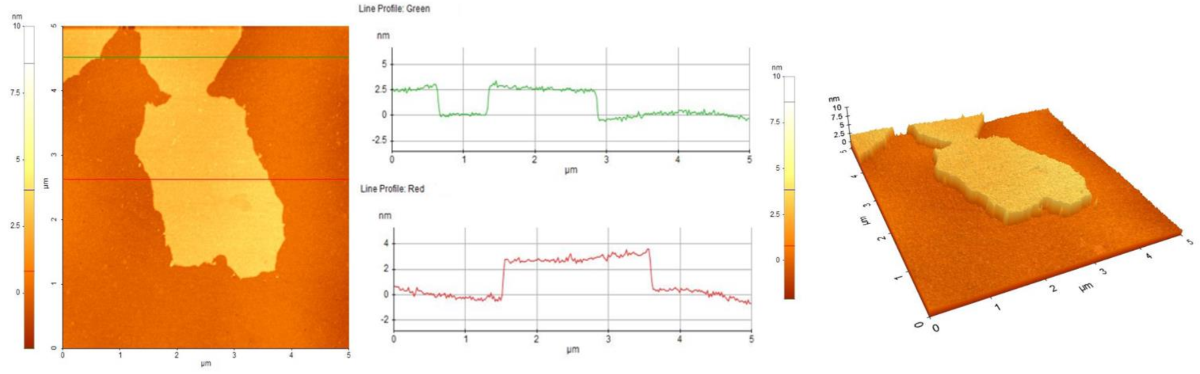

Figure S3. AFM image and its height profile of graphene flake deposited on the bare Si-wafer.

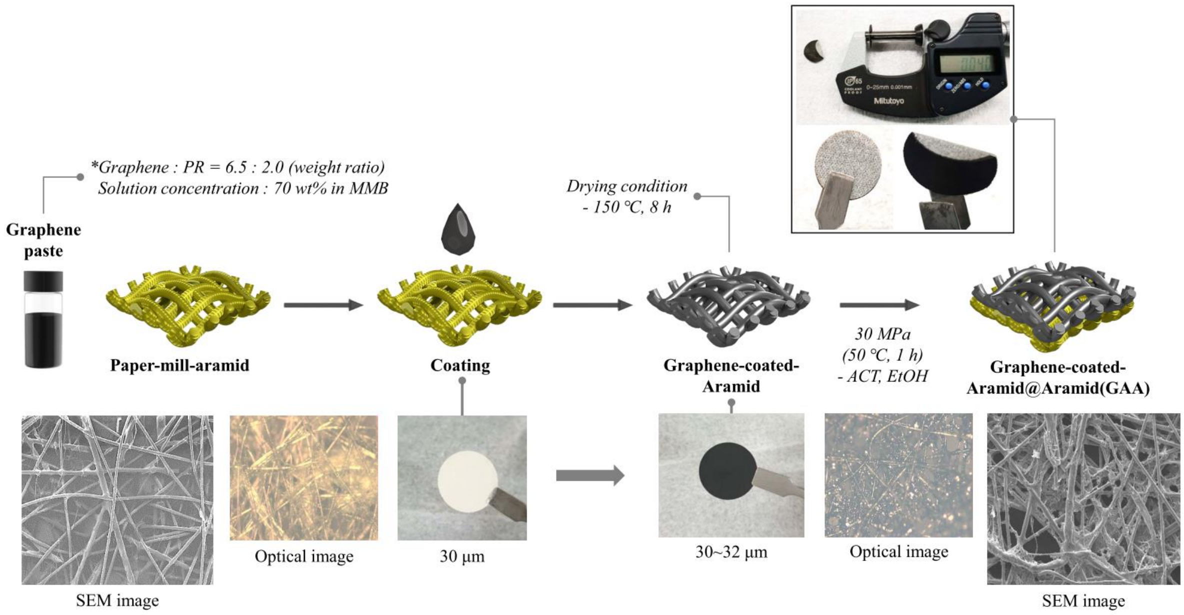

Figure S4. Fabrication process of GAA

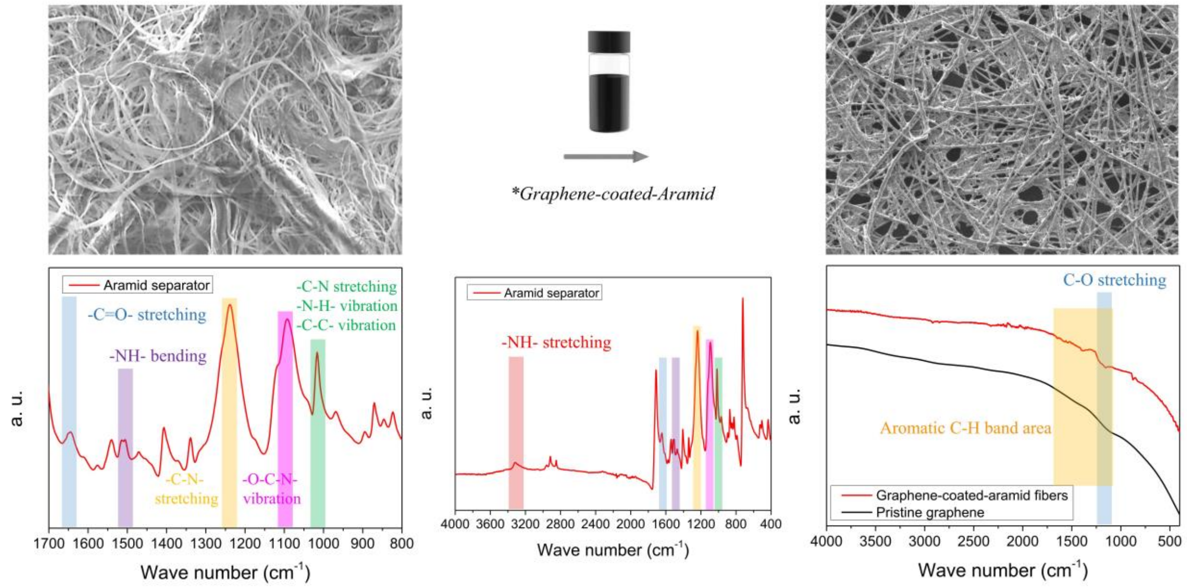

Figure S5. FT-IR analysis. Before the graphene paste coating, the typical aramid peaks (-C(=O)-N(-H)-) appears from 800 cm^{-1} to 1700 cm^{-1} and at 3300 cm^{-1}. After the graphene paste coating, the aramid peaks did not appear, and the spectrum similar to pristine graphene was observed in GAA (C−O peaks was shown by PR resin).[75,79-82]

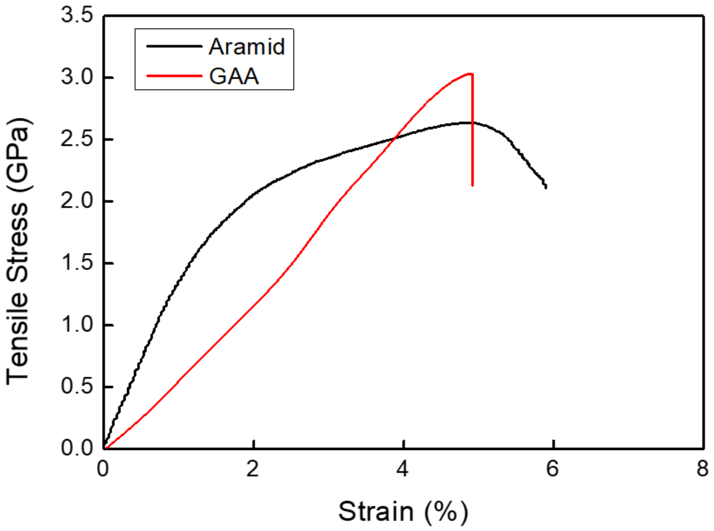

Figure S6. Mechanical property of the uncoated aramid and the graphene-coated-aramid.

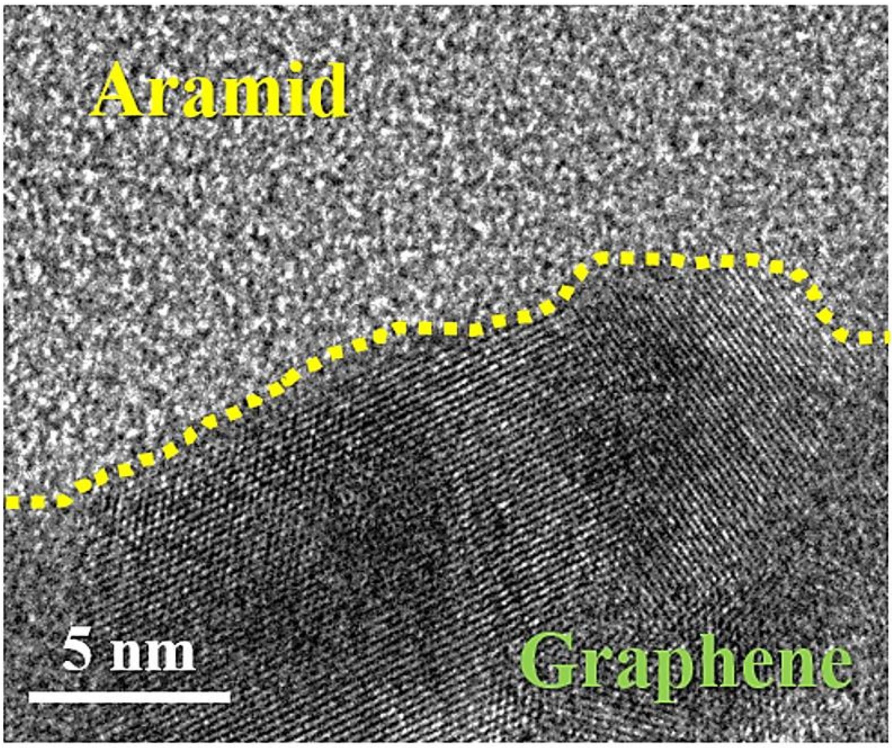

Figure S7. TEM image of the interface between aramid and graphene.

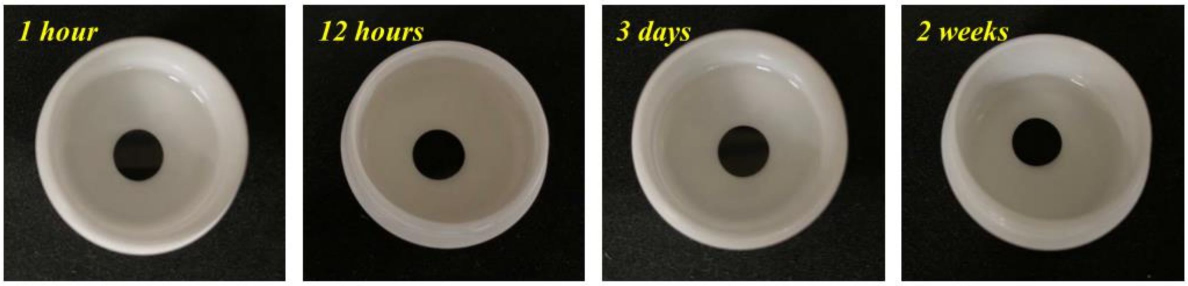

Figure S8. The solubility test of the graphene-coated-aramid side.

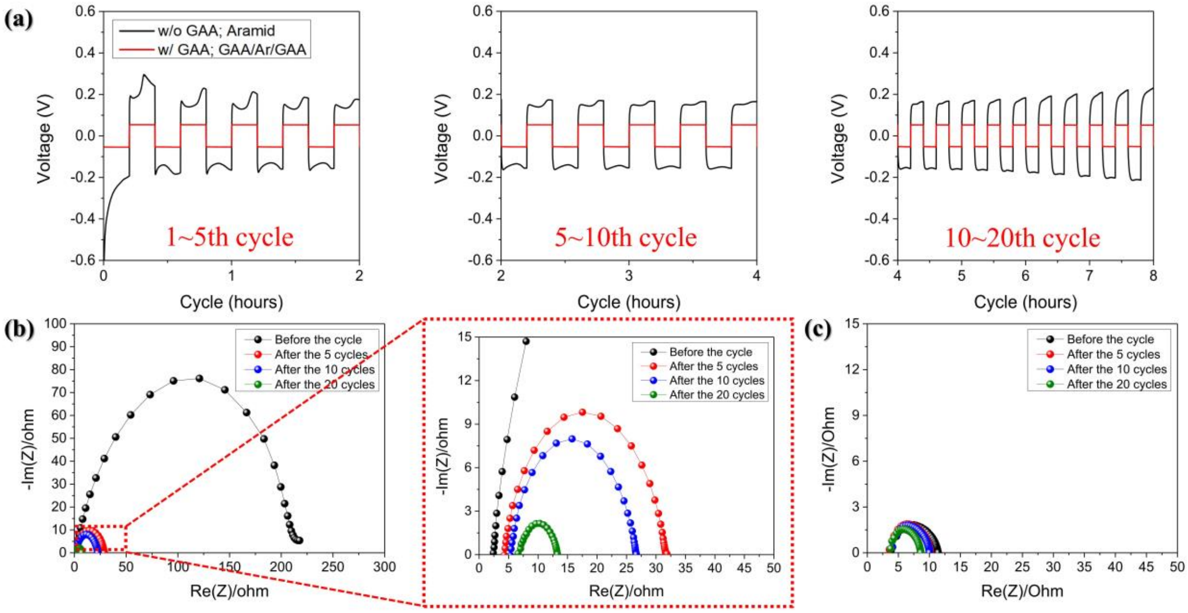

Figure S9. Electrochemical impedance spectroscopy (EIS) data. (a) The time-voltage profiles in initial stage (1 ~ 20th cycles). (b) EIS data of the reference system. (c) EIS data of the GAA applied system. The reference system indicates a high resistance (~220 Ω cm^{-2}) before the cycling. As cycle progresses, it was significantly decrease to 31.8 Ω cm^{-2} after the 5 cycles and to 26.6 Ω cm^{-2} after the 10 cycles and to 13.2 Ω cm^{-2} after the 20 cycles as a result of the native oxide layer destruction and the dendritic Li formation, while the GAA applied system showed a low resistance and a small decrease by the stable SEI formation at the initial stage; 11.4 Ω cm^{-2} before the cycling, 10.1 Ω cm^{-2} after the 5 cycles, 9.90 Ω cm^{-2} after the 10 cycles, 8.62 Ω cm^{-2} after the 20 cycles.[32]

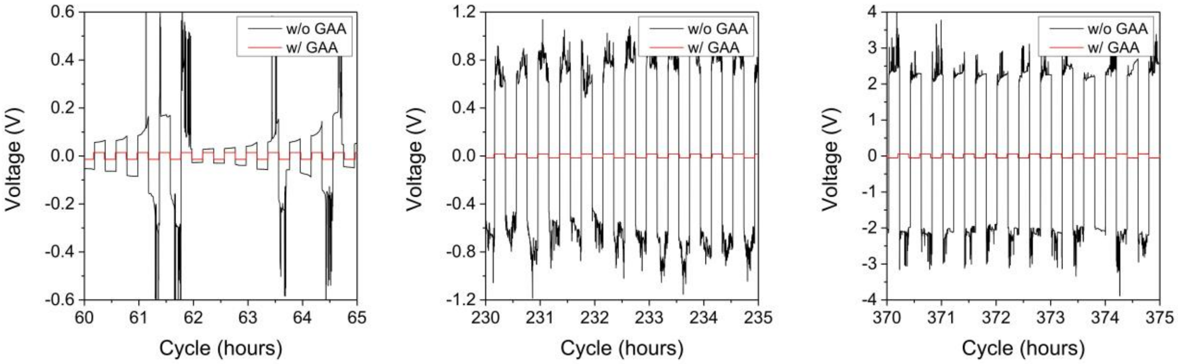

Figure S10. Anodic polarization curves in Li|Li symmetrical cell test as the cycle progresses. (5 mA cm^{-2}, 1 mAh cm^{-2})

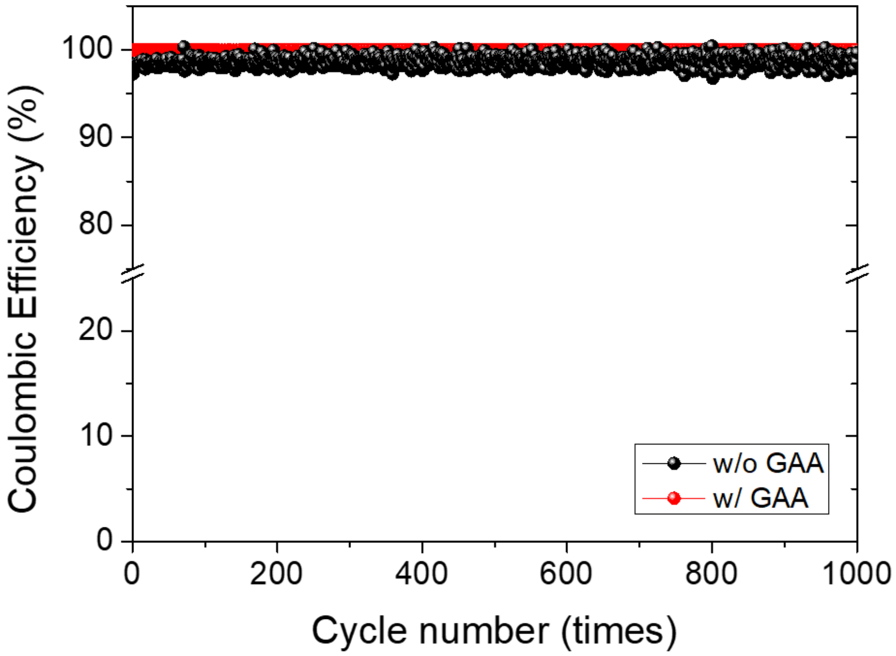

Figure S11. Coulombic efficiency of Li metal batteries with GAA separators (*sample*) and without GAA separators (*Ref.*).

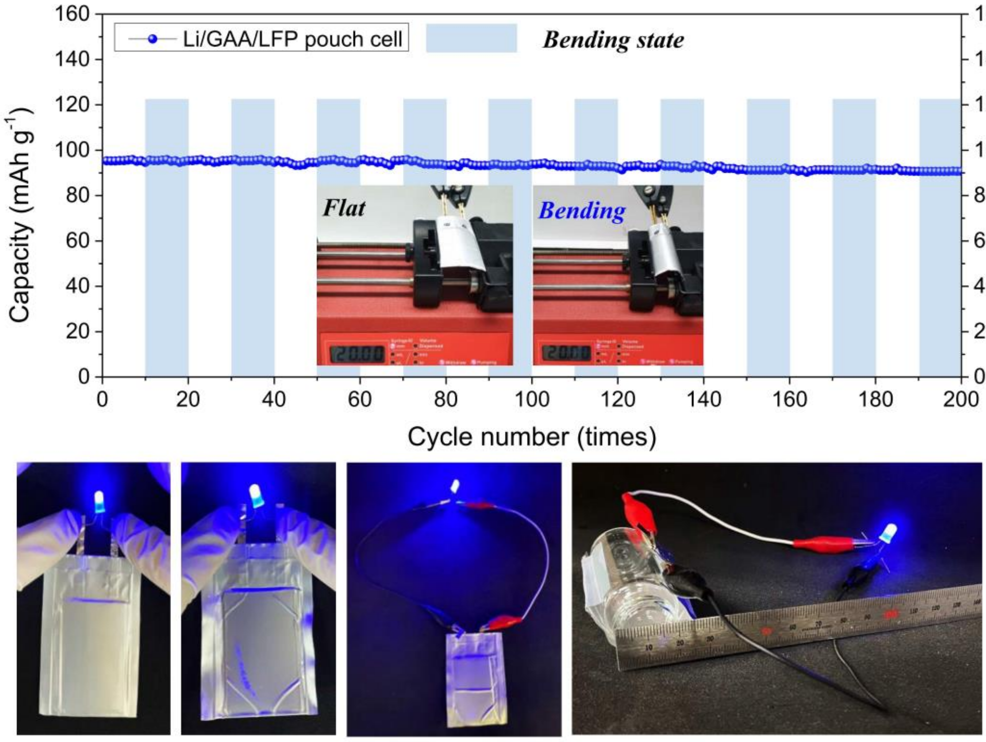

As-prepared *5 th bending* *10 th bending*

Figure S12. The cycling performance of the flexible Li metal battery with the GAA separators in the repeated dimensional change (at 20 C-rate, bending radius: 20 mm).

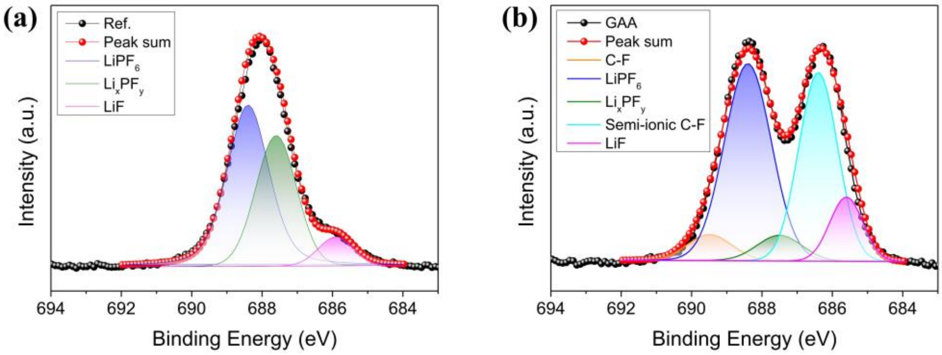

Figure S13. F XPS data.[71,83,84]

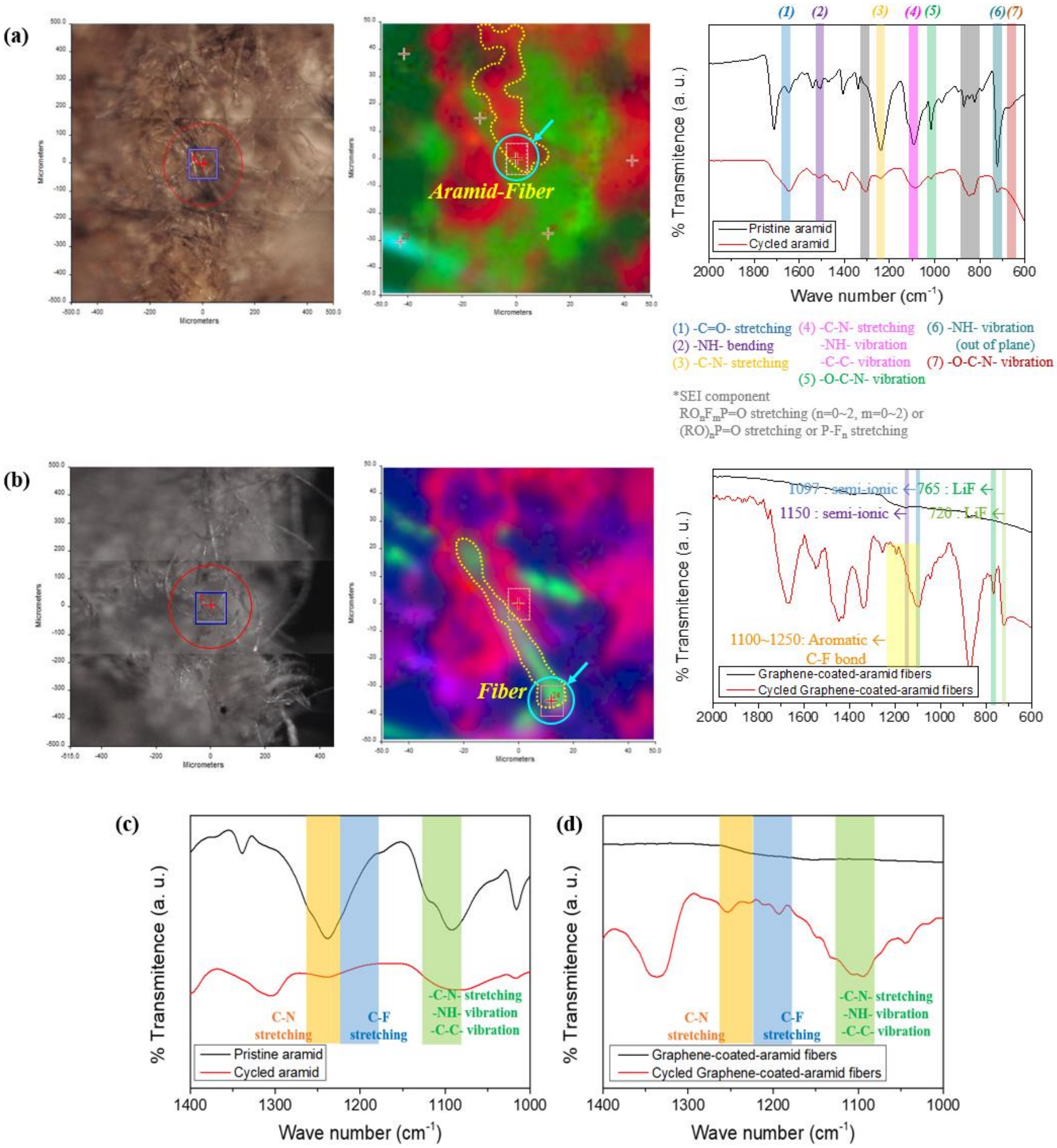

Figure S14. Microscopic FT-IR data of (a) the uncoated aramid fiber and (b) the graphene-coated-aramid fiber after the 1000 cycles in the current density of 5 mA cm^{-1} (1 mAh cm^{-1}). To reveal sections, fibers was cut in an oblique direction using the surface and interfacial characterizing analysis system (SAICAS). The analyses were focused on the red cross in the white dotted square line. [75,79-82,85-90] (c and d) The enlarged graph from 1000 ~ 1400 cm^{-1}.

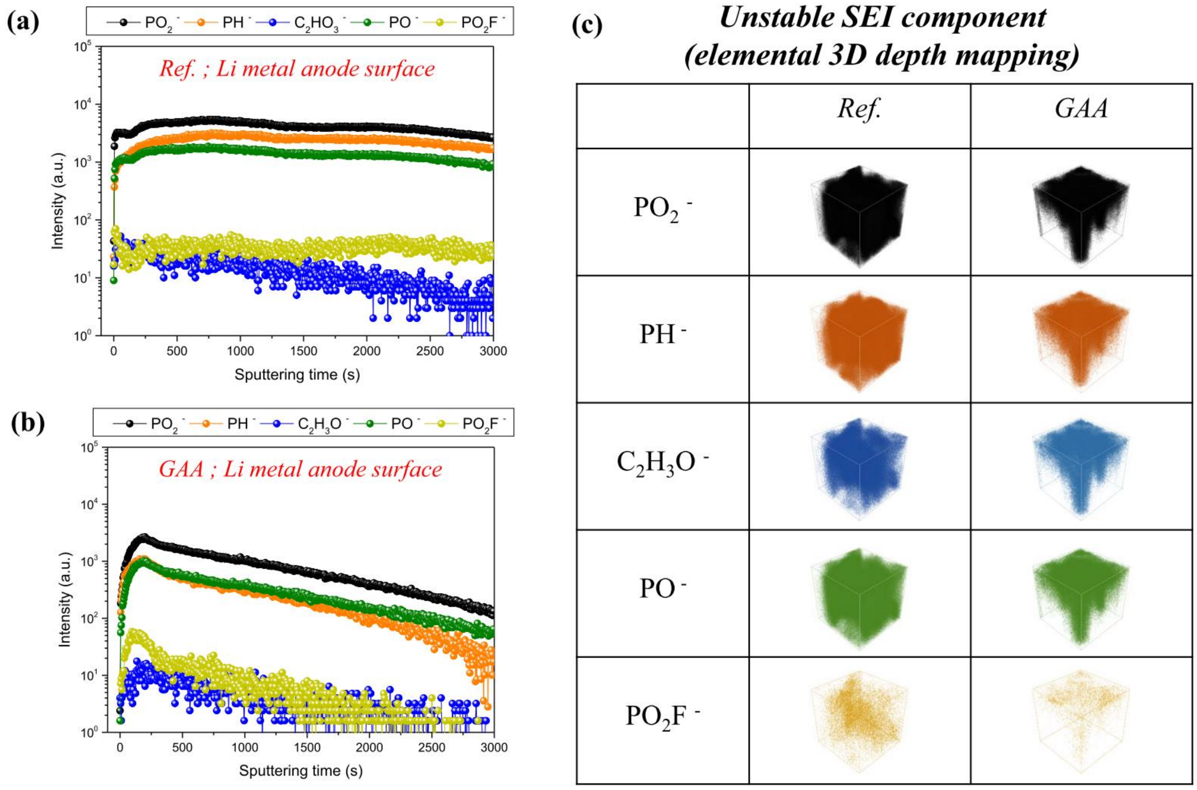

Figure S15. TOF-SIMS data. Depth profiles; (a) and (b), 3D depth mapping image; (c).

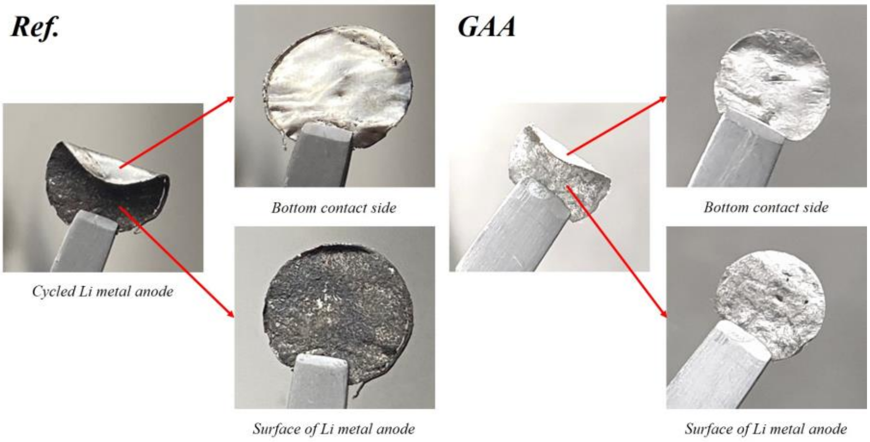

Figure S16. Optical image of Li metal anode before and after the cycle (1000 times at the current density of 5 mA cm^{-2} (1 mAh cm^{-2})).

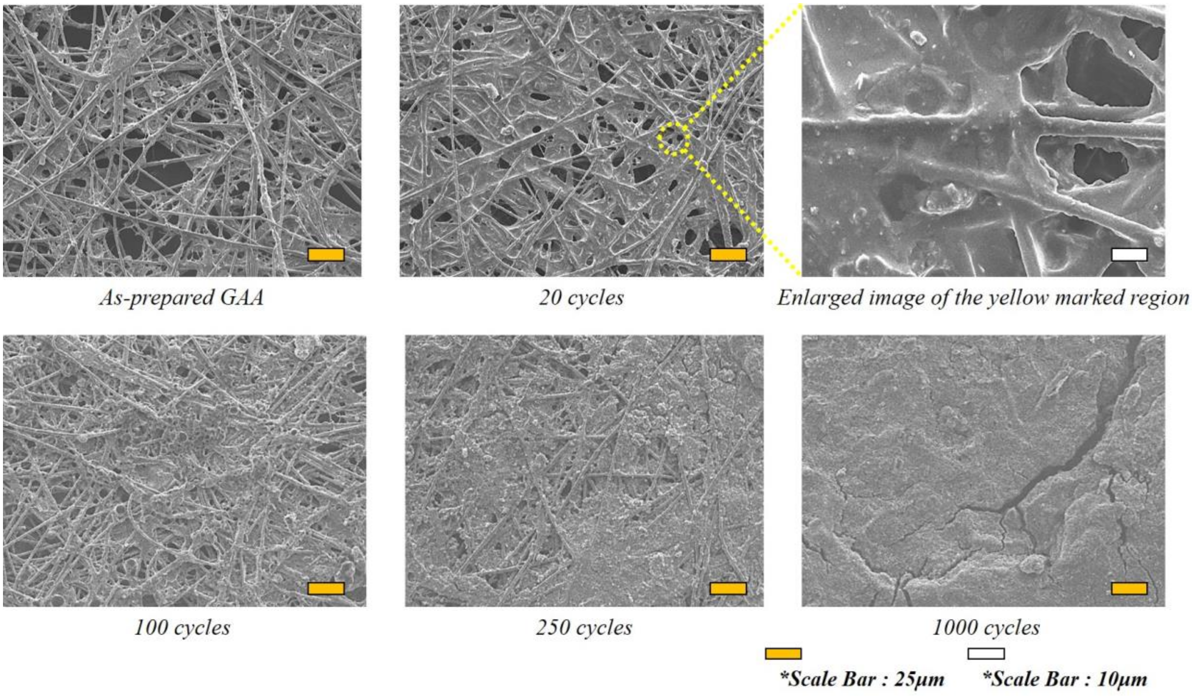

As-prepared GAA

20 cycles

Enlarged image of the yellow marked region

100 cycles

250 cycles

1000 cycles

Figure S17. SEM facial image of the graphene-coated-fiber side as cycle progresses.

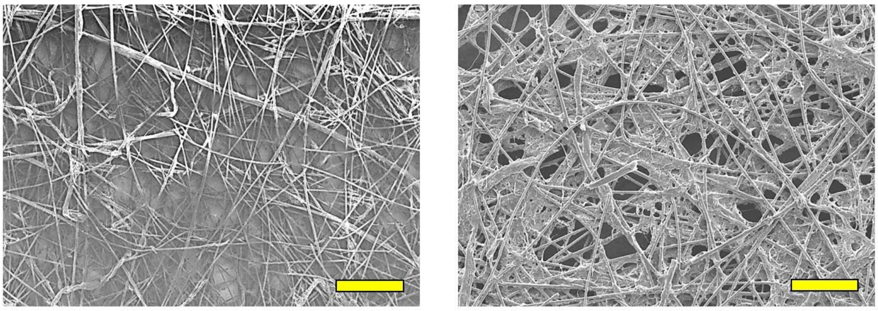

Pristine Aramid Paper *Graphene-coated-Aramid*

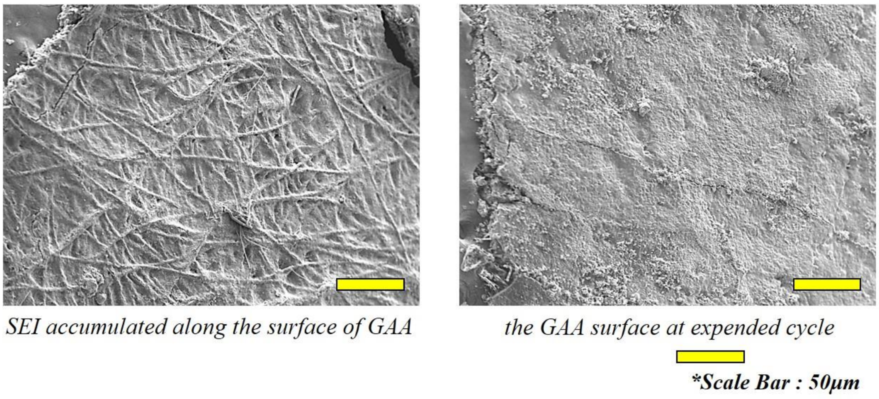

SEI accumulated along the surface of GAA *the GAA surface at expended cycle*

Figure S18. SEM oblique (45°) image of the graphene-coated-fiber side as cycle progresses.

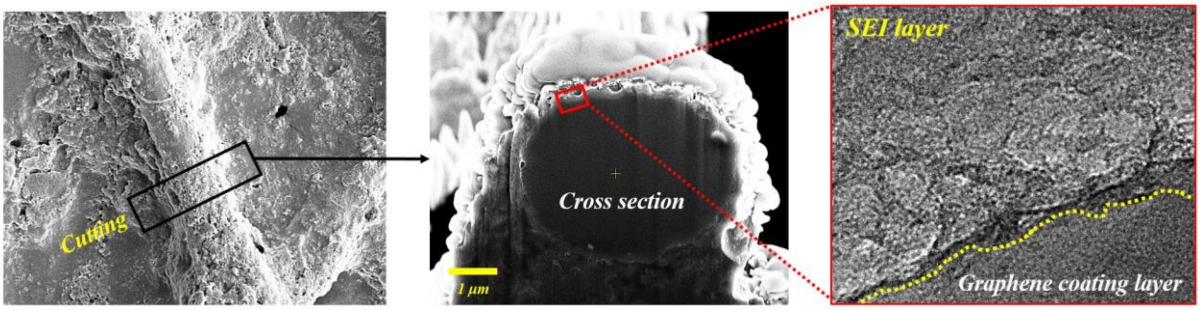

Figure S19. SEM cross section image of the cut fiber and the enlarged image of the boundary. The mosaic area around the graphene-coating-layer was considered as SEI.

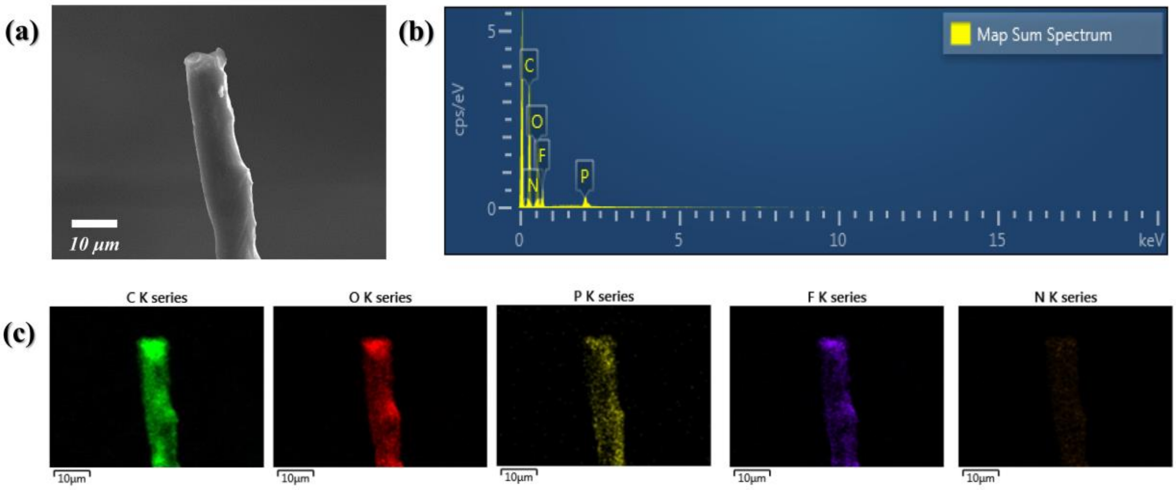

Figure S20. SEM analysis. (a) The single fiber strand image. (b) EDS data and (c) EDS mapping images of the single fiber strand of GAA after the cycle.

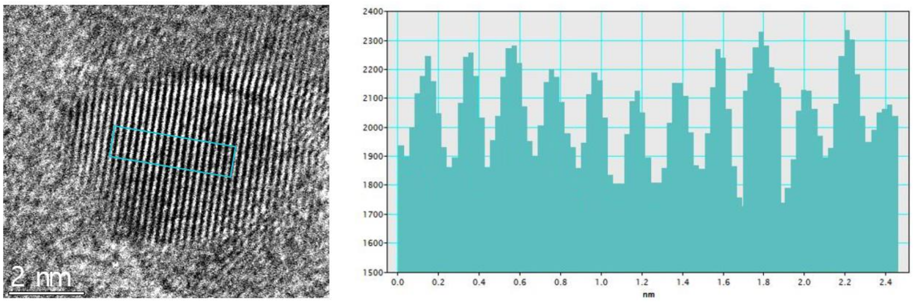

Figure S21. The internal spacing measurement of graphene using by Cs-STEM.

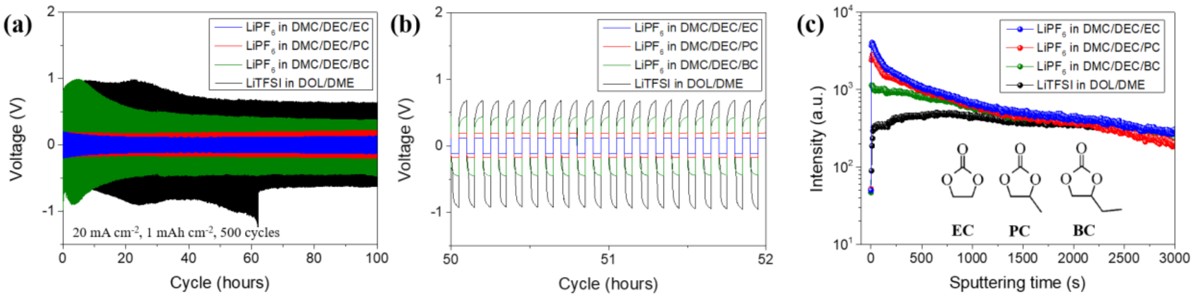

Figure S22. (a, b) Galvanostatic cycling measurement: the time-voltage profiles for Li|Li symmetrical cells in different solvent system. (c) The ratio of LiF$^-$ among TOF-SIMS data for the LMA surface of in different solvent system. To confirm the effects of solvent, the electrochemical data of the cells and the LiF ratio on the LMA surface is compared using ethylene carbonate (EC), propylene carbonate (PC), and 1,2-butylene carbonate (BC) (Polarity: EC > PC > BC, Size: EC < PC < BC, Dielectric constant: EC (90) > PC (65.5) > BC (56.1) at 300 K).[91,92] In addition, the different electrolyte system of LiTFSI in DOL/DME was also compared (DOL:1,3-dioxolane, DME: dimethyl ether). In a PC solvent introduced system, it showed a low ohmic potential drop and a stable anodic polarization curve, which means the stable operation of the cell. This is presumed that PC solvent has a similar role to EC solvent inside the cell environment. As a result, when PC was introduced, a relatively high proportion of LiF was formed on the surface of the Li metal anode, resulting in a stable SEI formation. However, when BC solvent was introduced, the time-voltage profile in the half cycle showed the arc shape plateau and the Li metal surface exhibited show a relatively low ratio of LiF. This is because the thick inactive layer as resistance factor made tortuous pathway across the electrode/electrolyte interphase to Li$^+$ ion migration, which means that the Li$^+$ ion transport was impeded by the thick inactive layer. So, the large concentration difference of Li$^+$ ion between the reducing electrode and the oxidizing electrode induces the change that the dominant kinetics became the mass transport in the expanded cycles. The interfacial concentration variation was accompanied by an overpotential increase, and then the dynamic concentration gradient reached its quasi-steady-state equilibrium with the arc shape plateau of the time-voltage profile in the half cycle.[36-38] From these results, it is assumed that BC solvent, which has a lower polarity, a larger size, and a lower dielectric constant than EC or PC, was not effective in stabilize PF_5 and less affected the F-doping mechanism. That is, in a BC solvent introduced system, the surface stability of Li metal is significantly low in comparison to EC or PC solvent introduced system.[36-38] Meanwhile, the electrolyte system of LiTFSI in DOL/DME shows an arc shape plateau similar to that of BC, and indicates a low LiF ratio on the surface of Li metal anode. This suggests that the mechanism of LiF formation via fluorine doping to graphene proposed in this study is difficult to be applied to the TFSI anion in DOL/DME system.

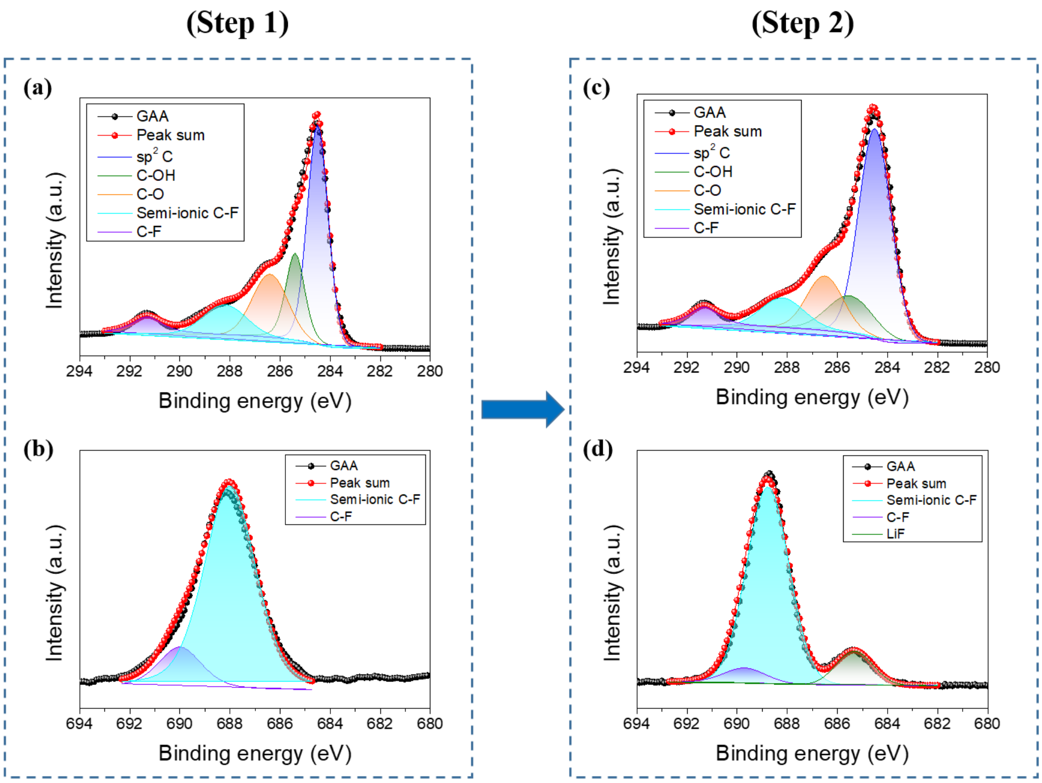

Figure S23. XPS data. (a) C XPS and (b) F XPS after F-doing process using HPF_6 in water. (c) C XPS and (d) F XPS after the Li salts treatment. An ex-situ experiment was conducted in an external water jacket by separation into two steps involving the partially fluorinated graphene and the LiF formation. It confirmed that LiF is formed by Li^+ ion flux after fluorine was doped; (i) The graphene coating layer was partially fluorinated using 1 M HPF_6 in water when the electrical field was applied. At this time, the graphene coating layer was used as the role of the anode for receiving electrons in the coin-cell and a platinum electrode was used as the counter electrode, and a current density of 5 mA was applied continuously for 8 hours. The platinum electrode should be used as the counter electrode because HPF_6 is a strong acid (pKa = −20 in water). In this process, water acts like an EC because it is also a polar, compact, and high dielectric constant solvent. (ii) After eight hours of the doping process, a sufficient amount of Li salt was melted in another water jacket filled with water. In this water jacket, the electrical field was applied to the F-doped graphene-coated aramid and the platinum electrode. The Li^+ ion flux migrates to the graphene coating layer while the anion of the Li salt migrates to the platinum electrode. During the experiment, the voltage was fixed at a value lower than the electrochemical window of the anion of Li salt to prevent the anionic decomposition of Li salt. As shown in XPS data, when the graphene coating layer goes through only step 1, the carbon-fluorine bonds appear in C XPS, but LiF does not appear in F XPS. The C–OH and C–O peaks is estimated to be due to the PR resin and the electrolysis of water. And, after the step 2, the carbon-fluorine bonds of C XPS and LiF peak in F XPS appear. Although the experiment was conducted in two steps, the result is the same as that of the manuscript. Through this result, it is possible to better understand the LiF formation by F-doping mechanism.

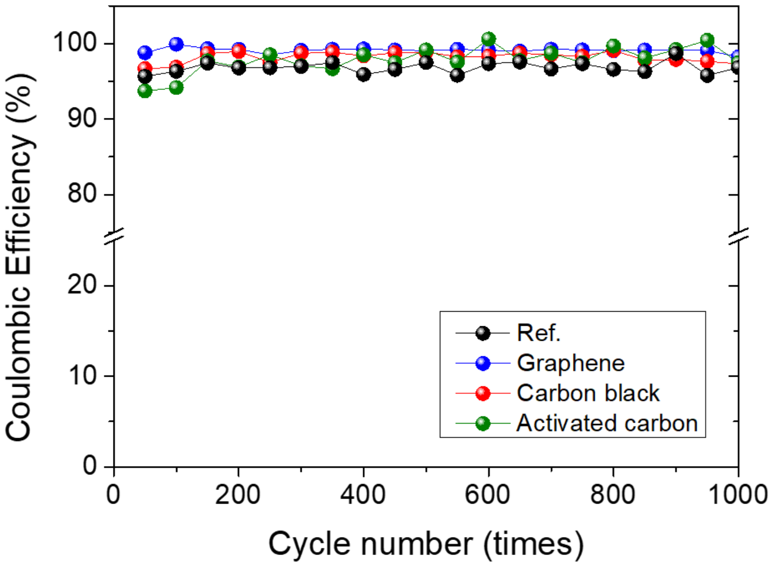

Figure S24. Coulombic efficiency of Li metal batteries in the case of the other CCN materials being applied.

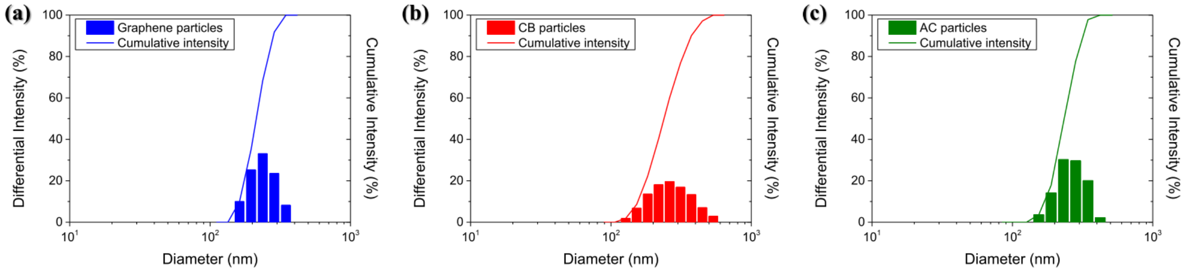

Figure S25. Particle size distribution of the carbon materials measured by dynamic light scattering spectrophotometer (DLS) after the grinding process; (a) Graphene. (b) Carbon black. (c) Activated carbon.

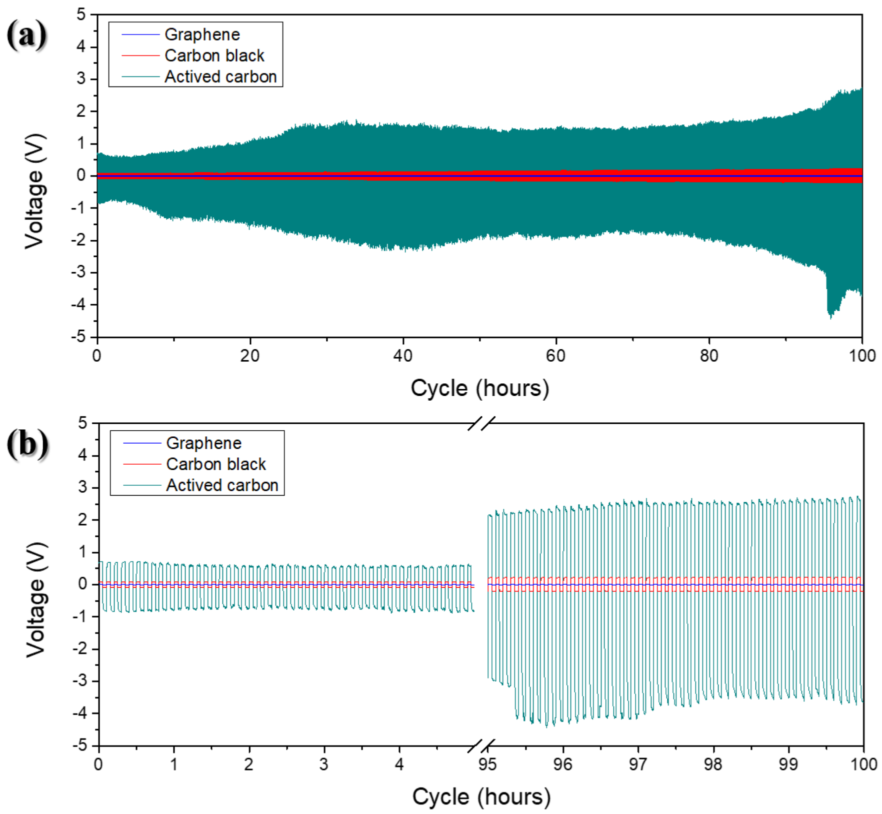

Figure S26. Li|Li symmetrical cell test at the high current density of 20 mA cm^{-1} (1 mAh cm^{-1}) in graphene, carbon black, and activated carbon applied system.

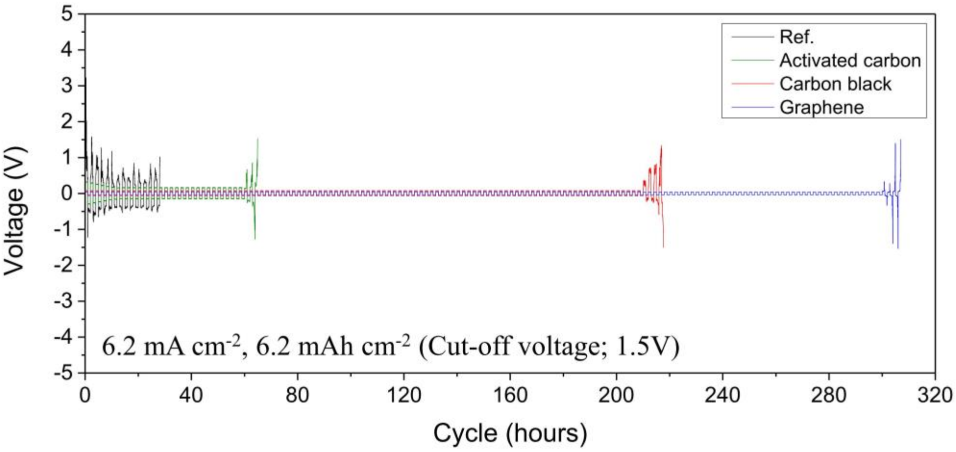

Figure S27. Life-span test.

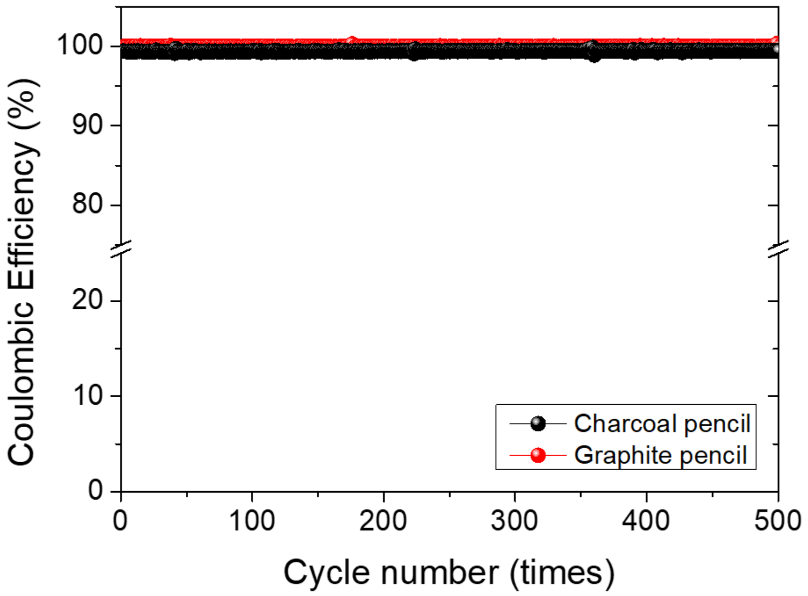

Figure S28. Coulombic efficiency of Li metal batteries in the case of the charcoal pencil and the graphite pencil applied.

[69] W. S. Hummers, R. E. Offeman, *J. Am. Chem. Soc.*, 1958, 80, 1339-1339.

[70] Q. Yun, Y.-B. He, W. Lv, Y. Zhao, B. Li, F. Kang, Q.-H. Yang, *Adv. Mater.*, 2016, 28, 6932.

[71] W. Feng, P. Long, Y. Li, *Adv. Sci.,* 2016, 3, 1500413.

[72] A. N. Enyashin, A. L. Ivanovskii, *Chem. Phys. Lett.,* 2012, 545, 78.

[73] T. Nakajima, *J. Fluor. Chem.,* 1999, 100, 57-61.

[74] T. Nakajima, M. Koh, V. Gupta, B. Žemva, K. Lutar, *Electrochimi. Acta,* 2000, 45, 1655–1661.

[75] P. Gong, Z. Wang, Z. Li, Y. Mi, J. Sun, L. Niu, H. Wang, J. Wang, S. Yang, *RSC Adv.,* 2013, 3, 6327.

[76] J. Kima, R. Zhou, K. Murakoshi, S. Yasuda, *RSC Adv.,* 2018, 8, 14152.

[77] T. Nakajima, *Macromol. Symp.,* 1994, 82, 19.

[78] U. Rajeena, M. Akbar, P. Raveendran, R. M. Ramakrishnan, *New J. Chem.,* 2018, 42, 9658.

[79] M. Mukherjee, S. Kumar, S. Bose, C. K. Das, A. P. Kharitonov, *Polymer-Plastics Technology and Engineering,* 2008, 47, 623.

[80] N. Sharma, V. Sharma, Y. Jain, M. Kumari, R. Gupta, S. K. Sharma, K. Sachdev, *Macromol. Symp.,* 2017, 376, 1700006.

[81] Y. Wang, W. C. Lee, K. K. Manga, P. K. Ang, J. Lu, Y. P. Liu, C. T. Lim, K. P. Loh, *Adv. Mater.,* 2012, 24, 4285.

[82] S. Abramowitz, N. Acquista, I. W. Levin, *J. Res. Natl. Bur. Stand. A phys. Chem.,* 1968, 72A, 487.

[83] T. Chen, X. Wang, Y. Liu, B. Li, Z. Cheng, Z. Wang, W. Lai, X. Liu, *Phys. Chem. Chem. Phys.,* 2017, 19,35504.

[84] C. Shen, S. Wang, Y. Jin, W.-Q. Han, *ACS Appl. Mater. Interfaces,* 2015, 7, 25441.

[85] Y. Okamoto, *J. Electrochem. Soc.,* 2013, 160, A404−A409.

[86] S. Leroy, F. Blanchard, R. Dedryvere, H. Martinez, B. Carre, D. Lemordant, D. Gonbeau, *Surf. Interface Anal.,* 2005, 37, 773−781.

[87] K. W. Schroder, H. Celio, L. J. Webb, K. J. Stevenson, *J. Phys. Chem. C,* 2012, 116, 19737−19747.

[88] D. E. Arreaga-Salas, A. K. Sra, K. Roodenko, Y. J. Chabal, C. L. Hinkle, *J. Phys. Chem. C,* 2012, 116, 9072−9077.

[89] R. Dedryve`re, S. Leroy, H. Martinez, F. Blanchard, D. Lemordant, D. Gonbeau, *J. Phys. Chem. B,* 2006, 110, 12986−12992.

[90] E. Pretsch, P. Buűhlmann, M. Badertscher, Structure Determination of Organic Compounds. In: IR Spectroscopy. Springer-Verlag Berlin Heidelberg, 2009.

[91] Y. Chernyak, *J. Chem. Eng. Data* 2006, 51, 416-418.

[92] L. H. Hess, A. Balducci, *Electrochimica Acta* 2018, 281, 437-444.